Spray freeze-drying for inhalable L-leucine, mannitol-based microparticles: The impact of process variables, L-leucine, and crystallinity on Aerosolization properties

Powder Technology 455 (2025) 120788

Contents lists available at ScienceDirect

Powder Technology

journal homepage: www.journals.elsevier.com/powder-technology

Spray freeze-drying for inhalable L-leucine, mannitol-based microparticles: The impact of process variables, L-leucine, and crystallinity on Aerosolization properties

Lorena Pasero [a], Adamo Sulpizi [b], Tomaso Guidi [b], Roberto Pisano [a,*]

[a] Department of Applied Science and Technology, Politecnico di Torino, 24 Corso Duca Degli Abruzzi, 10129 Torino, Italy
[b] R&D Department, Chiesi Farmaceutici S.p.A, Largo F. Belloli 11/A, 43122 Parma, Italy

HIGHLIGHTS

- Inhalable microparticles engineered by Spray Freeze-Drying.
- A Design of Experiments (DoE) model is used to achieve the optimal size.
- The relationship between size, crystallinity, and deposition is disclosed.
- Leucine favors deposition only when microparticles crystallinity is controlled.
- The optimal amount of leucine for lung deposition is proposed.

GRAPHICAL ABSTRACT

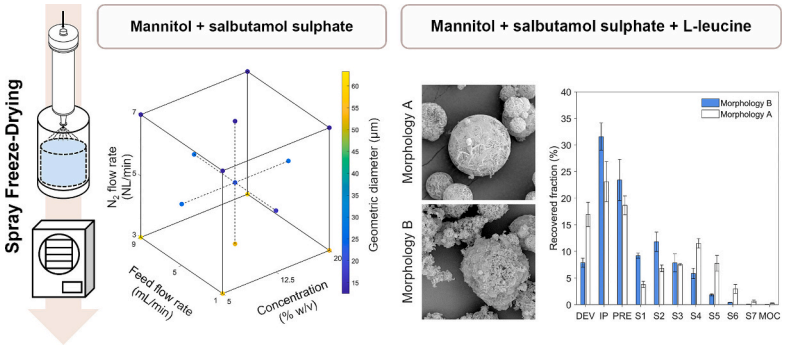

ARTICLE INFO

Keywords:
Spray freeze-drying
Inhalable microparticles
Inter-particle cohesiveness
Leucine
Polymorphism
Aerosolization

ABSTRACT

In this study, microparticles carrying salbutamol sulphate were produced by pneumatic spray freeze-drying. The optimal particle size was assessed through a model, associated with a design of experiments. Growing solid concentrations and N_2 flow rate led to decreasing geometric diameters, while an opposite effect was associated with the feed flow rate. The aerodynamic diameter, instead, increased at increasing solid concentrations. Moreover, the role of crystallinity in determining the microparticles' flowability was evaluated upon the incorporation of L-leucine. The addition of the amino acid induced the formation of two morphologies with different degrees of crystallinity. The absence of recrystallization significantly improved the aerosolization properties of the microparticles up to a maximum fine particle fraction (48 %) and a minimum mass median aerodynamic diameter (2 μm) at 10 % (*w/w* db) L-leucine. This result disclosed the influence of polymorphism on the microparticles' cohesiveness, proving the dependency of the microparticles' aerodynamics on L-leucine and mannitol crystallinity.

* Corresponding author.
E-mail addresses: lorena.pasero@polito.it (L. Pasero), a.sulpizi@chiesi.com (A. Sulpizi), t.guidi@chiesi.com (T. Guidi), roberto.pisano@polito.it (R. Pisano).

https://doi.org/10.1016/j.powtec.2025.120788
Received 17 June 2024; Received in revised form 7 February 2025; Accepted 10 February 2025
Available online 16 February 2025

1. Introduction

In the last decade, spray freeze-drying (SFD) has emerged as a cutting-edge technology for the manufacturing of temperature-sensitive pharmaceutics. This innovative technique combines the benefits of spray drying and freeze-drying to produce microparticles (MPs) with controlled size and shape, improved drug bioavailability, and enhanced dissolution [1]. SFD involves the atomisation of a solution into droplets, which are instantaneously frozen into a cryogenic liquid (e.g., N_2) and then dried under vacuum [2]. The formation and subsequent sublimation of ice crystals provide the MPs with a porous structure, constituted by an excipient-based matrix embedding the drug [3]. The high porosity of such MPs reduces their mass density, thus making them extremely aerodynamically performant [4]. Therefore, SFD represents a promising approach to producing drugs to be administered through dry powder inhalers (DPI), which require optimum aerodynamic properties to deposit in the target site of the lung and exert their action [5]. Size, mass density, and shape are the main factors affecting the aerodynamic diameter (d_{ae}) of an MP, i.e., the diameter of a sphere with the same settling velocity and unitary density [6]. The d_{ae} is recognized as the most crucial feature in determining the aerodynamic performance of inhalable MPs, and it should be comprised between 1 and 5 μm to guarantee an appropriate fine particle fraction (FPF) [7]. The spherical shape of spray freeze-dried MPs is also suitable for inhalation purposes since it allows for higher FPFs compared to needle- and plate-shaped MPs [8].

SFD can fulfil such requirements by producing carrier-free MPs with relatively large geometric size and low mass density ($\sim$ 0.1 g/cm^3), namely large porous particles (LPPs). This technique has been applied to different drugs, including budesonide [9], voriconazole [10], salmeterol xinafoate [11], cefixime [12], and antibodies [13]. The matrix of LPPs is commonly composed of sugars, such as mannitol [14], trehalose [13], raffinose [12], and sucrose [15]. Among them, mannitol is widely employed due to its high mannitol-ice eutectic temperature and its crystallinity, which enhances powders' stability in DPIs [16]. Although SFD proved to be an appropriate technology to produce LPPs [14], reaching high FPF remains technically challenging. Owing to their surface energy and electrostatic properties, spray freeze-dried MPs have proven to be exposed to inter-particle cohesiveness which can affect their flowability [17]. Moreover, these powders are extremely sensitive to humidity-induced deterioration due to their great hygroscopicity. To overcome these obstacles, the inclusion of hydrophobic amino acids into the formulation has been proposed. Particularly, L-leucine (LL) has been shown to reduce both the hygroscopicity [12] and the inter-particle surface forces [9] of MPs, improving the flowability of DPI powders. Although LL effectively increases the dispersion of spray-dried and spray freeze-dried MPs by accumulating on their surface [12], its mechanism of action remains controversial. Li et al. identified the increased surface roughness induced by the presence of a crystalline LL shell as the cause of enhanced FPF in spray-dried MPs [18]. In spray drying processes, LL crystallisation starts during drying due to its progressive increase in concentration up to exceeding its solubility [19]. Beyond the surface tension, LL crystallisation is considered responsible for its enrichment on the MPs' surface since LL crystals have lower diffusion coefficient than dissolved LL, thus leading to an increased Peclet number [20]. In SFD, the supersaturation is induced by the cooling of the droplet and, even though a layer of LL may be present on the surface due to its lower surface tension and high surface activity [21], LL is also likely to crystallise from the bulk of the solution. Therefore, the formation of a crystalline LL shell is less probable in SFD than spray drying. Instead, the reduction in surface energy and cohesion forces among spray freeze-dried MPs, and their increase in surface potential were proposed as LL's prevalent effects in SFD [17].

In this study, pneumatic SFD was employed to produce inhalable microparticles composed of mannitol and salbutamol sulphate (SS). A design of experiments was conducted to comprehensively analyse the influence of the solid concentration, the atomisation gas flow rate, and the feed flow rate on the particle size. Most studies in the field of SFD have only focused on the individual impact of these variables, while here their interaction was considered, and a model was proposed. Furthermore, LL was incorporated into the formulation to increase the MPs' flowability, assessing the LL optimal content to reach the highest FPF. This work also aimed to shed light on the modification of the MPs' crystallinity either by varying the process conditions or upon the addition of LL. Indeed, whilst the influence of solid concentration and feed flow rate on mannitol crystallinity has been investigated for ultrasonic SFD [14], little is known about pneumatic SFD. Lastly, the relationship between the crystallinity of mannitol and LL MPs and their aerodynamic behaviour was uncovered, providing further information about the mechanism of action of this amino acid. To the best of our knowledge, this is the first study addressing the relationship between LL crystallinity and the flowability of spray freeze-dried powders.

2. Materials and methods

2.1. Formulations

Spray freeze-dried MPs were produced from different aqueous solutions at a concentration of 5, 12.5, and 20 % (*w/v*) of solute. D-mannitol ($C_6H_{14}O_6$, 98 + %. Chem-Lab NV, Zedelgem, Belgium) either (F1) alone or (F2) added with 1 % (*w/w* db) SS ($C_{13}H_{21}NO_3{\cdot}0.5H_2SO_4$, Teva Pharmaceutical Industries Ltd., Israel) was employed. F2 was then added with LL ($C_6H_{13}NO_2$, Sigma-Aldrich, St. Louis, MO, USA) at (F3) 5, (F4) 10, and (F5) 20 % (*w/w* db), maintaining a total solute content of 5 % (*w/v*). All the formulations involved in this study are listed in Table 1.

2.2. Spray freeze-drying

Spray freezing (SF) into vapour over liquid was used to produce frozen MPs. A syringe pump (Model KDS 200, KD Scientific, Holliston, MA) was used to convey the solution to a two-fluid nozzle (B-290, Ø0.7 mm, Buchi, Flawil, Switzerland), placed at approximately 10 cm above a Dewar containing liquid N_2. During atomisation, the sprayed MPs were maintained under gentle agitation by a magnetic stirrer placed inside the Dewar. Then, the frozen MPs were collected into a beaker, covered with a Phase Separator 1 PS (Whatman, Maidstone, UK) and put into a freeze-dryer prechilled at −50 °C. Primary drying was conducted at 10 °C and 20 Pa, while secondary drying was performed at 20 °C and 20 Pa for 5 h. The end of primary drying corresponded to the unitary ratio between the pressures detected by a Pirani and a capacitance (Baratron®, MKS, Andover, MA, USA) manometer. Following drying, the resulting powders were transferred into vials, sealed, and stored over silica gel in a desiccator at room temperature.

2.3. Particle size and morphology

Particle size and morphology were investigated by scanning electron microscopy (SEM) after one week of storage. The spray freeze-dried powders were first spread over the surface of a double-sided carbon tape (NEM TAPE, Nisshin LTD, Tokyo, Japan), stuck on top of an aluminium stub. Then, the carbon tape was coated with platinum for 20

Table 1
List of the formulations involved in the study. F1 and F2 were produced at 5, 12.5, and 20 % (*w/v*) solute concentration, while F3-F5 at 5 % (*w/v*).

	Solid (% *w/v*)	Mannitol (% *w/w* db)	SS (% *w/w* db)	LL (% *w/w* db)
F1	5, 12.5, 20	100	–	–
F2	5, 12.5, 20	99	1	–
F3	5	94	1	5
F4	5	89	1	10
F5	5	79	1	20

s at 30 mA through a sputter coater Quorum Q150T S (2 M Instruments, Rome, Italy). Image acquisition was conducted at 15 kV voltage using a Desktop SEM Phenom XL (Waltham, MA, USA). For each sample, the open-source ImageJ software (NIH, Bethesda, MD, USA) was then used to determine the geometric diameter (d_g) of 400 MPs. The particles' d_{ae} was calculated as follows:

$$d_{ae} = d_g\sqrt{\frac{\rho}{\rho_a \lambda}} \tag{1}$$

where ρ is the particle mass density, ρ_a is the unitary mass density (1 g/cm^3), and λ is the shape factor (equal to 1 for spheres). ρ was estimated as:

$$\rho = \rho_f \tag{2}$$

where ρ_f is the concentration (w/v) of solid in the feedstock solution. The formalisation of Eq. (2) is provided in the 'supporting information'. For each set of 400 MPs, the geometric and aerodynamic sizes were expressed as the mean diameter ± the standard deviation (SD). The dimensional homogeneity of the powders was also expressed by the span value:

$$\text{Span} = \frac{D_{90} - D_{10}}{D_{50}} \tag{3}$$

where the diameters D_{90}, D_{10}, and D_{50} correspond to the sizes at which, respectively, 90 %, 10 %, and 50 % of the MPs' population is smaller.

2.4. Karl Fischer titration analysis

The residual moisture of the powders was measured by Karl Fischer titration (KF Coulometer type DL32, Metter Toledo, Novate Milanese, Italy). About 50–100 mg of powder was dissolved in 2–3 mL of Karl Fischer reagent. This mixture was then injected into the Karl Fischer titrator cell, where it reacted with the titration reagent under magnetic stirring. The water content of the sample was calculated based on its dried weight. Measures were performed in triplicate.

2.5. Surface tension

Surface tension measurements were performed through a drop shape analyser (Krüss, Hamburg, Germany) using the pendant drop method [22]. Briefly, a droplet was generated through a 0.5 mm needle and its image was acquired by a UI-3060CP-M-HQ R2 camera (IDS imaging, Obersulm, Germany). The surface tension, γ, was obtained by fitting the droplet profile with the Young-Laplace equation:

$$\gamma\left(\frac{1}{R_1}+\frac{1}{R_2}\right) = \Delta P = \Delta P_0 - \Delta\rho g z \tag{4}$$

where R_1 and R_2 are the principal radii of curvature of the droplet, ΔP is the Laplace pressure at the interface, $\Delta\rho = \rho_d - \rho_c$ is the difference between the density (ρ_d) of the droplet and the density (ρ_c) of the continuous phase (air), g is the gravitational constant, and z is the cylindrical coordinate of the system (see Fig. 1). ΔP_0 is the Laplace pressure at $z = 0$. For each formulation, ten droplets were analysed, and the results were expressed as the mean ± the SD.

2.6. X-ray diffraction

The crystalline structure of MPs was investigated by powder X-ray diffraction (PXRD) employing an X-ray diffractometer (Empyrean, Malvern Panalytical, Malvern, UK) after one week of storage. The analysis was performed between 5° and 60° with a 2θ step size of 0.026°, at 40 mV and 40 mA. The X'pert Highscore software (Malvern Panalytical, Malvern, UK) was used to examine the diffraction spectra. For all the formulations, three characteristic peak ratios ($R_{\delta/\beta}$, $R_{\alpha/\beta}$, $R_{\alpha/\delta}$) were considered:

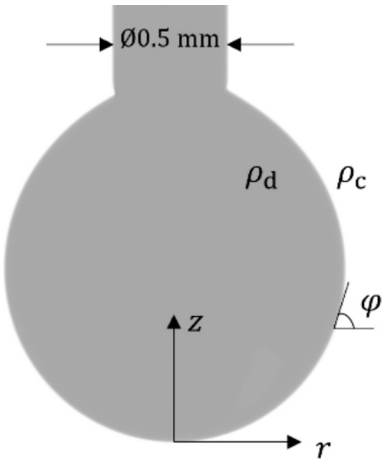

Fig. 1. Schematic of a pendant droplet under a needle (0.5 mm diameter). z and r are the cylindrical coordinates, while φ is the tangent angle of the droplet. ρ_d and ρ_c are the density of the droplet and air, respectively.

$$R_{\delta/\beta} = \frac{I_{22.06^\circ}}{I_{23.4^\circ}} \tag{5}$$

$$R_{\alpha/\beta} = \frac{I_{17.3^\circ}}{I_{23.4^\circ}} \tag{6}$$

$$R_{\alpha/\delta} = \frac{I_{17.3^\circ}}{I_{22.06^\circ}} \tag{7}$$

where $I_{22.06^\circ}$, $I_{23.4^\circ}$, and $I_{17.3^\circ}$ represent the intensity of the peak at 22.06°, 23.4°, and 17.3°, respectively. Instead, an additional peak ratio ($R_{\delta/LL}$) was considered for the formulations F3-F5 as follows:

$$R_{\delta/LL} = \frac{I_{22.06^\circ}}{I_{5.94^\circ}} \tag{8}$$

where $I_{5.94^\circ}$ is the intensity of the peak at 5.94°.

2.7. Nucleation time of solid in vapour phase

During freezing, the nucleation of solid in the atomised droplets may start either in the vapour or in the liquid phase depending on the properties of both the freezing environment and the droplets. To better understand this phenomenon, here, the nucleation time t_n of solid inside an atomised droplet was calculated as follows:

$$t_n = \frac{d_g \rho_d C_v}{6h} ln\left[\frac{T_i - T_\infty}{T_n - T_\infty}\right] \tag{9}$$

where h is the heat transfer coefficient, C_v is the specific heat at constant volume of the droplet, T_n and T_i are, respectively, the nucleation and initial temperature of the droplet, and T_∞ is the ambient temperature (N_2 gas). T_i was assumed equal to 25 °C, T_n was taken as −20 °C [23], while T_∞ (−104 °C) was measured in the N_2 gas phase by using a thermocouple. The formalisation of Eq. (9) is provided in the 'supporting information'. According to [23], the heat transfer coefficient was determined by the correlation:

$$Nu = 2.0 + 0.6\, Re^{0.5} Pr^{0.33} = \frac{h d_g}{k^v_{N_2}} \tag{10}$$

Substituting the mathematical expression of Re and Pr in Eq. (10):

$$\frac{h d_g}{k^v_{N_2}} = 2.0 + 0.6\left(\frac{\rho^v_{N_2} v_s d_g}{\mu^v_{N_2}}\right)^{0.5}\left(\frac{c_{p_{N_2}} \mu^v_{N_2}}{k^v_{N_2}}\right)^{0.33} \tag{11}$$

and

$$h = \frac{k^{v}_{N_2}}{d_g}\left[2.0 + 0.6\left(\frac{\rho^{v}_{N_2} v_s d_g}{\mu^{v}_{N_2}}\right)^{0.5}\left(\frac{c_{p^{v}_{N_2}}\mu^{v}_{N_2}}{k^{v}_{N_2}}\right)^{0.33}\right] \quad (12)$$

where $k^{v}_{N_2}$, $\rho^{v}_{N_2}$, $\mu^{v}_{N_2}$, and $c_{p^{v}_{N_2}}$ are the thermal conductivity, the density, the viscosity, and the specific heat capacity of the N_2 vapour phase, respectively. These physical properties were taken from the Perry's Chemical Engineers' Handbook [24], using N_2 gas data at T_∞. v_s, instead, represents the slip velocity of the droplet assumed equal to 10 m/s [23].

2.8. In vitro drug deposition

The powders containing SS (F2-F5) were analysed through a Next Generation Impactor (NGI) (Copley, Nottingham, UK) to assess their aerodynamic properties and in vitro drug deposition. The NGI was connected to a critical flow controller TPK (Copley, Nottingham, UK) and a rotary pump SCP5 (Copley, Nottingham, UK). Before each dispersion, the stages of the NGI were covered with 1 % TWEEN® 20 to prevent particle bouncing and the pre-separator was filled with 15 mL of water, as recommended by the British Pharmacopeia. For each sample, a hydroxypropyl methylcellulose capsule (Vcaps Plus, size 3, transparent cap and body, Capsugel®, Lonza Group, Basilea, Switzerland) was loaded with the powder and inserted into a high-resistance RS01® DPI device (RPC Plastiape®, Osnago, Italy). In detail, dispersions were performed in triplicate at 60 L/min for 3.8 s. After each dispersion, the powders were collected from device (capsule, inhaler, and adapter; DEV), induction port (IP), pre-separator (PRE), NGI cups (S1–S7), and micro-orifice collector (MOC) by rinsing with 25, 50, 100, 10, and 10 mL of water, respectively. The solutions derived from the MOC underwent filtration using a 0.45 μm PTFE filter. Then, each solution was examined by high-pressure liquid chromatography (Acquity UPLC®, Waters™, Milford, CT, USA) and data were collected with the Copley Inhaler Testing Data Analysis software (CITDAS) (Copley, Nottingham, UK). The sum of SS mass detected in the device and NGI apparatus returned the recovered dose (RD). The ratio between the RD in each stage and the total RD represented the recovered fraction (RF). The emitted fraction (ED) was expressed as the sum of SS collected in the NGI. The ratio between the mass of powders with a d_{ae} less than 5 μm and ED gave the fine particle fraction (FPF). Finally, the mass median aerodynamic diameter (MMAD) and the geometric standard deviation (GSD) were provided by CITDAS from the particle size distributions. The MMAD represents the particle size which categorises the MPs population in two halves, while the GSD expresses the polydispersity index of an aerosol [25].

2.9. Design of experiments

To assess the influence of different operating variables and their mutual interactions, a design of experiments was performed. As reported in Table 2, three operative conditions were selected as independent variables, i.e., solid concentration (x_1), N_2 flow rate (x_2), and feed flow rate (x_3), at three levels.

The mean d_g and d_{ae} were, instead, chosen as dependent response variables, namely y_1 and y_2. The experiments were conducted according to the face centered design (FCD) matrix reported in Table 3. This design consisted of a 2^3 factorial design (runs 1–8), 6 star points (runs 9–14), and a centre point (run 15). Runs 1–8 were replicated twice, while three replicates of run 15 were performed to lower the leverage of the model. The experiments listed in Table 3 were performed for the formulations F1 and F2.

A central composite design is commonly associated with a second-order polynomial equation (Eq. (12)), accounting for linear (x_i), interaction ($x_i x_j$), and quadratic (x_i^2) terms. According to this model, each response variable (y_u) is linked to each term by a coefficient (b_i, b_{ij}, b_{ii}) as follows:

$$y_u = b_0 + \sum_{i=1}^{k} b_i x_i + \sum_{\substack{i,j=1 \\ i\neq j}}^{k} b_{ij} x_i x_j + \sum_{i=1}^{k} b_{ii} x_i^2 \quad u = 1, 2 \quad (12)$$

where b_0 is the intercept and k is the number of dependent variables, i.e., 3. The column matrix of coefficients ($\boldsymbol{B}$) is obtained as following:

$$\boldsymbol{B} = \left[\boldsymbol{X}^{T}\boldsymbol{X}\right]^{-1}\left[\boldsymbol{X}\right]^{T}\boldsymbol{Y} \quad (13)$$

where $\boldsymbol{X}$ is the design matrix and $\boldsymbol{Y}$ is the column matrix of the responses. Here, the Chemometric Agile Tool (CAT, R. Leardi, C. Melzi, G. Polotti, freely downloadable from http://gruppochemiometria.it/index.php/software) was employed to obtain the coefficients of the model and to validate it at x_1, x_2, and x_3 equal to −1, 0.5, and − 1 (5 % (*w/v*), 6 NL/min, and 1 mL/min), respectively.

2.10. Statistical analysis

CAT was employed to determine the statistical significance of the model's coefficients by an analysis of variance (ANOVA) for quadratic model. The one-way ANOVA tool of the SIGMA Plot software's data analysis was performed to compare the d_g of F3-F5. $p < 0.001$, $p < 0.01$, and $p < 0.05$ were considered significant.

3. Results and discussion

3.1. Particle morphology

3.1.1. Morphology of F1-F2 MPs

Fig. 2 shows the SEM images of F1-F2 MPs. For both formulations, the cohesiveness among MPs dramatically increased as their size decreased, particularly for growing N_2 flow rates. Indeed, smaller sizes are commonly associated with larger surface areas available for surface

Table 2
Variables and levels of the FCD conducted for F1 and F2. The unit NL/min refers to standard conditions related to 0 °C and 1013.25 mbar abs, and is the unit displayed on the flowmeter used to control N_2 flow rate (Q-Flow 140, Vögtlin Instruments GmbH, Muttenz, Switzerland).

Level	Concentration (% *w/v*)	N_2 flow rate (NL/min)	Feed flow rate (mL/min)
−1	5	3	1
0	12.5	5	5
1	20	7	9
Variable	x_1	x_2	x_3

Table 3
Matrix of the FCD conducted for F1 and F2.

Run #	x_1	x_2	x_3
1	−1	−1	−1
2	−1	1	−1
3	−1	−1	1
4	−1	1	1
5	1	1	1
6	1	1	−1
7	1	−1	1
8	1	−1	−1
9	−1	0	0
10	1	0	0
11	0	0	1
12	0	0	−1
13	0	1	0
14	0	−1	0
15	0	0	0

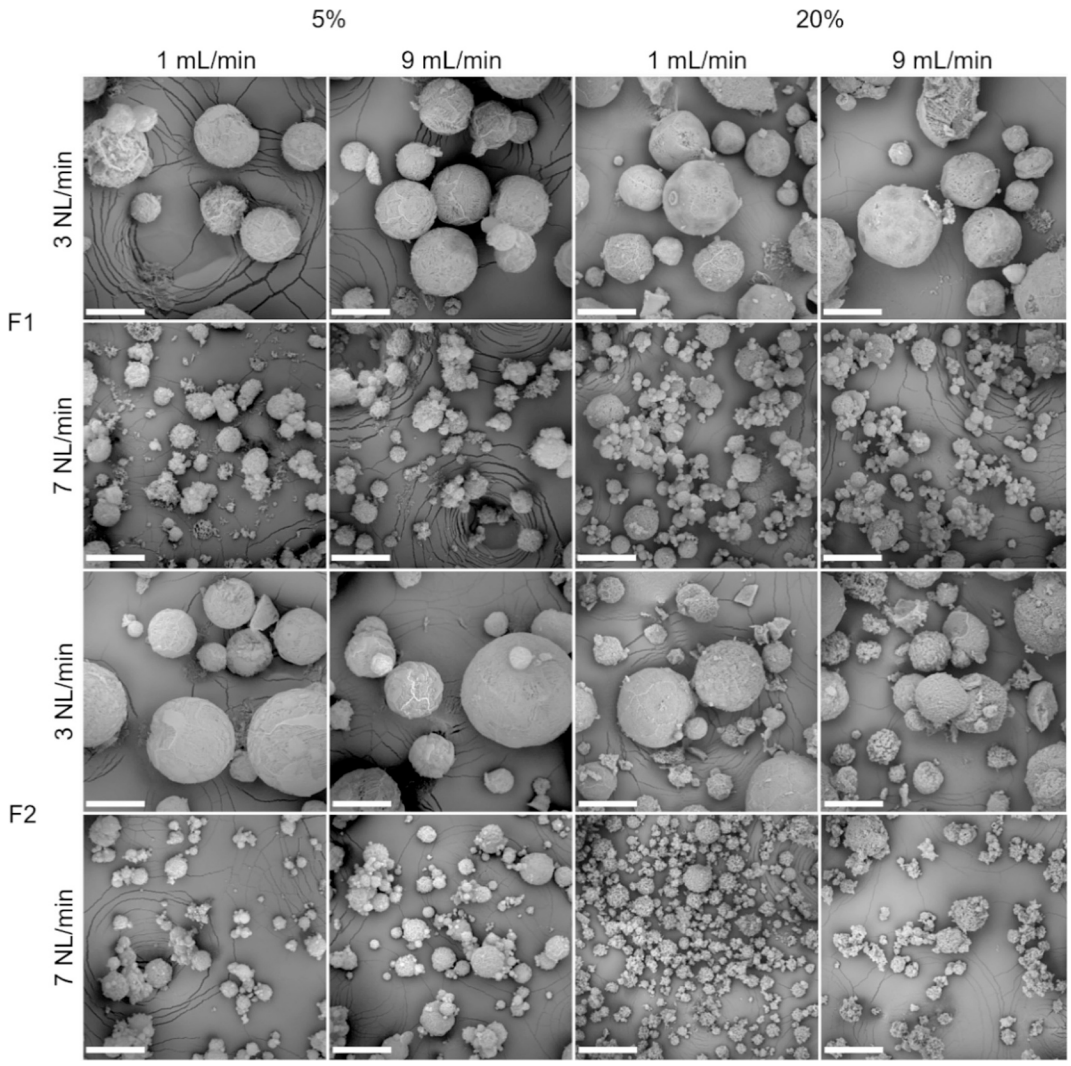

Fig. 2. SEM images of MPs, produced at 5, 20 % (*w/v*) of solid (F1 and F2), 3, 7 NL/min of N_2 flow rate, and 1, 9 mL/min of feed flow rate. Scale bars refer to 100 μm and 640× magnification.

charge transfer, resulting in stronger cohesion forces among MPs [8]. Such inter-particulate cohesiveness is a well-known issue in DPI formulation since it may induce poor powder flowability [8]. Therefore, LL was added to the formulation F2 to limit the MPs' cohesiveness.

3.1.2. Morphology of F3-F5 MPs

As reported in Fig. 3, F3-F5 MPs maintained a spherical shape and the traditional porous structure of spray freeze-dried MPs. However, two different morphologies were formed for F3 and F5 after one week of storage: one displaying a smooth well-defined shape and the other with a corrugated irregular surface. For the sake of clarity, from now on we will refer to these morphologies as 'morphology A' and 'morphology B', respectively. Morphology B-based MPs displayed high inter-particulate cohesion, while this phenomenon was not induced by the presence of morphology A which was the only one exhibited by F4 MPs. [26] The reduction of cohesiveness in morphology A could be related to the exposure of LL hydrophobic chains on the surface of the MPs, which could limit the inter-particle interactions [26]. Furthermore, LL may reduce the surface energy of the MPs, similar to the effect observed in spray-dried MPs containing trileucine. [27] The transition from morphology A to B may have been triggered by a recrystallisation during storage, as addressed in Section 3.3.2.

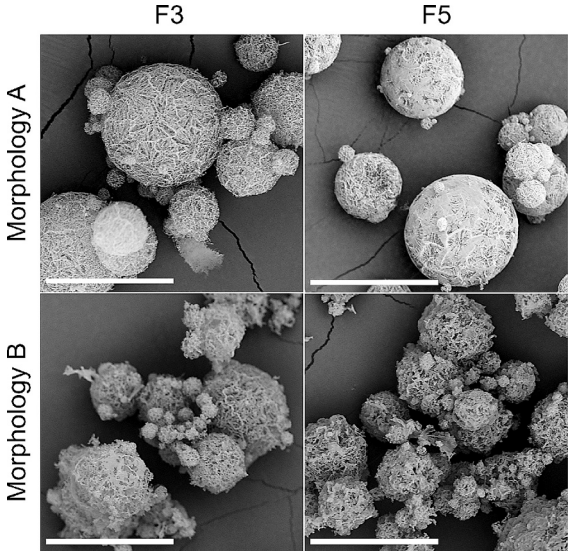

Fig. 3. SEM images of MPs containing 5 (F3) and 20 % (*w/w* db) (F5) of LL. MPs were produced at 5 % (*w/v*) of solid, 7 NL/min of N_2 flow rate, and 9 mL/min of feed flow rate. Scale bars refer to 50 μm and 1450× magnification.

3.2. Particle size

3.2.1. F1-F2 size optimisation via DoE

For both formulations F1 and F2, a model was used to assess the relationship between the mean d_g (y_1) and d_{ae} (y_2) and the three operative variables, i.e., solid concentration (x_1), N_2 flow rate (x_2), and feed flow rate (x_3). Fig. 4 graphically represents the coefficients of the model for different formulations and response variables. For all the conditions, x_2 had a negative effect on y_1 and y_2, while x_3 had a positive effect. Instead, x_1 was inversely and directly correlated with y_1 and y_2, respectively. For F1 the following models were obtained:

$$y_1 = 25.2 - 3.6x_1 - 25.7x_2 + 4.9x_3 - 0.7x_1x_2 + 0.7x_1x_3 - 3.3x_2x_3 + 4.9x_1^2 + 14.5x_2^2 + 0.6x_3^2$$

where b_1 and b_{23} were significant at $p < 0.01$, while b_2, b_3, and b_{22} at $p < 0.001$, and:

$$y_2 = 8.8 + 3.7 - 8.8 + 1.7x_3 - 3.1x_1x_2 + 0.8x_1x_3 - 1.1x_2x_3 + 0.4x_1^2 + 5.2x_2^2 + 0.3x_3^2$$

where b_1, b_2, b_3, b_{12}, and b_{22} were significant at $p < 0.001$, while b_{23} at $p < 0.05$. For F2, instead, the models were:

$$y_1 = 21.9 - 0.1x_1 - 21.7x_2 + 3.1x_3 + 0.9x_1x_2 + 2.6x_1x_3 - 0.7x_2x_3 + 4.2x_1^2 + 10.2x_2^2 - 1.04x_3^2$$

where b_2 was significant at $p < 0.001$, b_{22} at $p < 0.01$, while b_3, b_{13} at $p < 0.05$, and:

$$y_2 = 7.8 + 3.8x_1 - 7.2x_2 + 1.3x_3 - 2.1x_1x_2 + 1.2x_1x_3 - 0.4x_2x_3 + 0.9x_1^2 + 3.5x_2^2 - 0.5x_3^2$$

where b_1, b_2, b_{12} were significant at $p < 0.001$, b_3 and b_{22} at $p < 0.01$, and b_{13} at $p < 0.05$.

The models were then tested at a random point of the domain, as reported in Fig. 5. The excellent agreement between the experimental and the predicted values validated the model for both response variables and formulations (see Fig. S1 of 'Supporting information). Therefore, a model predicting the mean d_g and d_{ae} of spray freeze-dried MPs composed of mannitol either alone or added with 1 % (*w/ w* db) SS was developed for the given experimental domain.

Figs. 6 and 7 illustrate the contour plots of the mean d_g and d_{ae} of MPs produced according to the FCD of F1 and F2, respectively. The influence of the solid content, the N_2 flow rate, and the feed flow rate on the particle size was assessed by employing an ANOVA for quadratic model to evaluate the statistical significance of each effect (see Table S1 of 'Supporting information').

For F1, the MPs' size was significantly influenced by the atomisation gas flow rate ($p < 0.001$), whose increase led to a dramatic reduction of the mean d_g owing to the intense shear stresses [28]. In detail, the particle size distributions of d_g were considerably shifted towards lower values upon the increase of the N_2 flux (see Fig. S2 of 'supporting information'). The geometric size also decreased by increasing the solid concentration ($p < 0.01$), while it increased for growing feed flow rates ($p < 0.001$). Overall, F2 exhibited lower mean d_g than F1 maintaining the same trends, except for the not statistically significant influence of the solid content and the lower significance of the feed flow rate ($p < 0.05$). Moreover, F2 displayed higher span values than F1, indicating a greater polydispersity of the powders (see Fig. S2 of 'supporting information'). For F1, the effects of the feed flow rate depended on the level of N_2 flow rate due to the strong interaction between these factors ($p < 0.01$). Indeed, at 7 NL/min the effect of the N_2 flow rate predominated, while the other contributes were smoothened. Instead, F2 showed a significant interaction between solid concentration and feed flow rate ($p < 0.05$). For F1, the lowest mean d_g was achieved at 7 NL/min combined with 20 % (*w/v*) solid (Fig. 6 *top left*). The combination of high N_2 flux and low feed flow rate provided the lowest geometric size for F2 (Fig. 7 *top right*). Being directly related to d_g (Eq. (1)), the mean d_{ae} was significantly influenced by the solid content ($p < 0.001$), the N_2 flow rate ($p < 0.001$), and the feed flow rate (F1: $p < 0.001$, F2: $p < 0.01$) for both formulations. However, an increase of d_{ae} was induced by growing solid concentrations due to the higher mass density (Eq. (1)). The N_2 flow rate significantly interacted with the solid concentration ($p < 0.001$ for F1 and F2) and the feed flow rate ($p < 0.05$ for F1). Additionally, a statistically significant interaction between concentration and feed flow rate ($p < 0.05$) was detected for F2. The lowest mean d_{ae} was around 4.5 μm for F1 and 2.2 μm for F2, both obtained at 7 NL/min, 5 % (*w/v*) solid and 1 mL/min.

Measurements of γ were performed to assess the effect of the solid content on the particle size distribution. As reported in Table 4, both formulations F1 and F2 exhibited reduced γ by increasing the solid content from 5 to 20 % (*w/v*). This result could explain the decreased mean d_g at growing solute concentration since a lower γ is generally responsible for a smaller droplet size during atomization [28]. Moreover, a decreasing γ was observed moving from F1 to F2 for all solid contents. Again, this result was coherent with the reduction of the mean d_g induced by the presence of SS (see Fig. S2 of 'supporting information'), which was more intense as the Δγ was higher (at 5 % (*w/v*)).

3.2.2. Size of F3-F5 MPs

The FCD foregrounded low solid concentration, high N_2 flow rate, and low feed flow rate as requirements of a pneumatic SFD process aimed at reducing the MPs' d_{ae}. Nevertheless, high feed flow rates were preferable to lower ones since they allowed for a shorter atomisation step, hence limiting the probability of nozzle clogging. Therefore, the combination of 5 % (*w/v*) solid, 7 NL/min of N_2 flow rate, and 9 mL/min of feed flow rate was highlighted as the optimal one to achieve the lowest d_{ae}, ensuring appropriate operating conditions. The addition of different amounts of LL was studied in these conditions and the resulting mean d_g are illustrated in Fig. 8. The inclusion of the amino acid appeared to decrease the particle size only when morphology B was formed, and this result was confirmed by the particle size distributions (see Fig. S3 of 'supporting information'). Coherently with previous studies [29], the addition of LL to 5 % (*w/v*) F2, reduced γ from 61.6 ± 0.8 mN/m to 59.0 ± 0.7 and 57.8 ± 0.4 mN/m for F3 and F5, respectively (Table 4). However, the one-way ANOVA evidenced a statistically significant ($p < 0.001$) decrement of d_g moving from morphology A to B for F3 and F5, while no difference was found comparing the same morphology at different LL concentration. Therefore, the reduction of d_g in LL-based MPs could be reasonably associated with the different morphology rather than the varied γ. The reduction of size of morphology B might have been caused by a shrinkage of MPs induced by either a polymorphic transition of mannitol or a different crystallisation of LL inside the porous matrix.

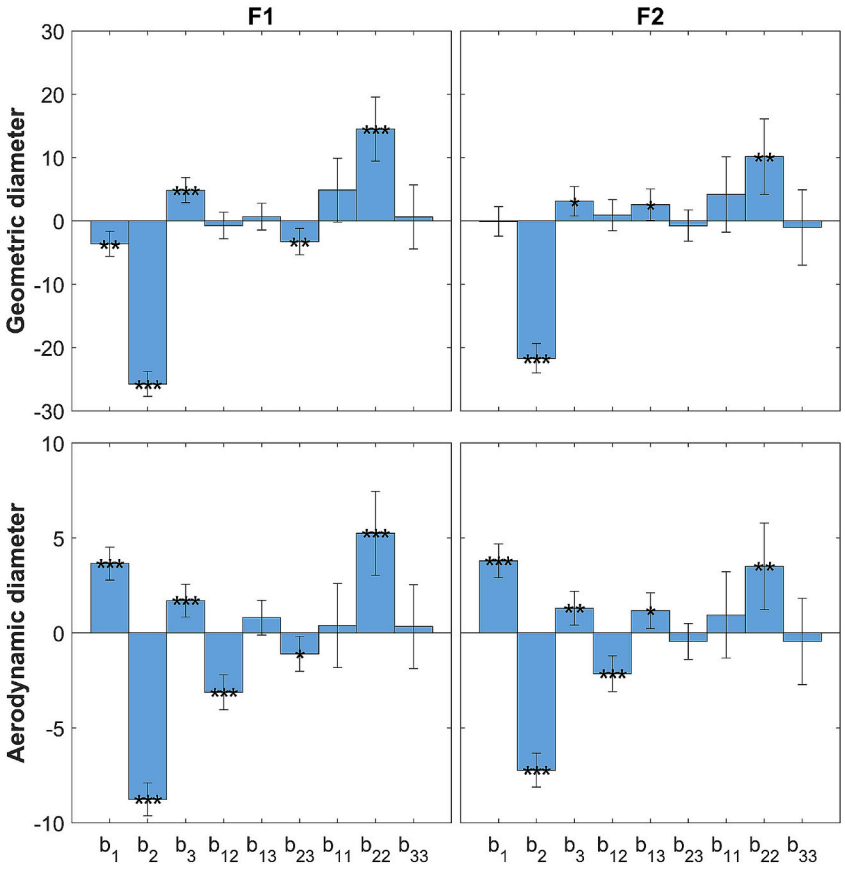

Fig. 4. A visual representation of the coefficients of the models for the two responses of the FCD, for the formulations F1 and F2. The brackets correspond to the confidence intervals at $p = 0.05$, while the stars indicate the significance of the coefficient (*: $p < 0.05$, **: $p < 0.01$, ***: $p < 0.001$).

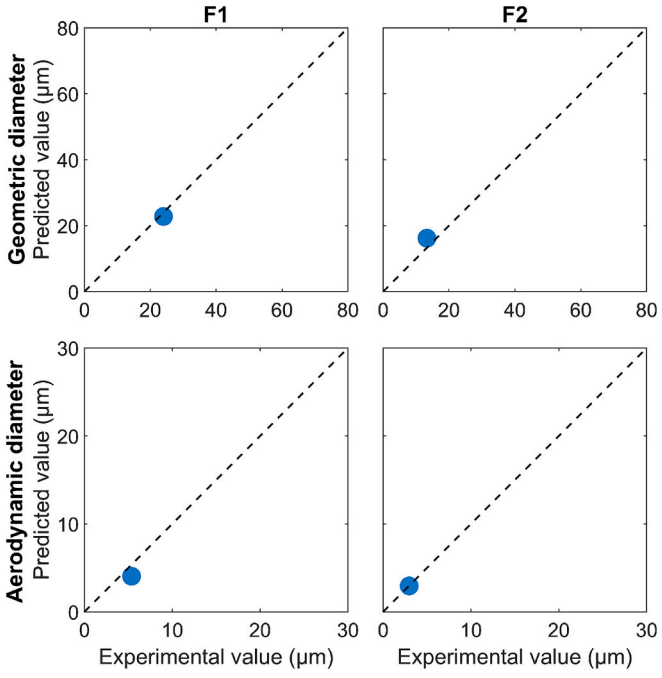

Fig. 5. A representation of the models' validation for the two responses of the FCD, for the F1 and F2 formulations.

3.3. Crystalline properties

3.3.1. Crystallinity of F1-F2 MPs

Being mannitol and LL crystalline excipients, PXRD analyses were conducted to investigate the crystalline structure of MPs. As discussed above, SEM imaging revealed the existence of two F2 MPs' morphologies, characterised by either rod-shaped or needle-like crystals (Fig. 2). This could be ascribable to the formation of different mannitol polymorphs during SFD, namely α-, β-, and δ-mannitol, or its hemihydrate form [30]. To understand the influence of the operative conditions on MPs' polymorphism, the PXRD spectra of F1 and F2 powders were examined (see Fig. S4 and Fig. S5 of 'supporting information'). For all the investigated conditions, δ-mannitol peaks were present at 9.7°, 22.06°, and 44.8°, β-mannitol peaks were observed at 14.6° and 23.4°, and lower amounts of α-mannitol were also detected at 17.3°. Although the shape of the spectra was not altered neither by the operative conditions nor by the formulation adopted, a variation of the peak intensity was observed. Most MPs were prevalently composed of δ-mannitol, generated by the transition from the stable β-polymorph (raw mannitol, see Fig. S6 of 'supporting information') to the metastable form δ due to the rapid freezing [14]. Indeed, the most stable polymorph forms following subsequent transitions through the least stable polymorphs according to the Ostwald's rule [31]. Here, the rapid freezing could have hindered the formation of β-polymorph since the molecules did not have enough time to arrange into the most stable structure. Moreover, the formation of δ-mannitol is favoured by the great supercooling degree due to its lower critical excess free energy than α or β [32]. By contrast, F2 MPs produced at 20 % (*w/v*) solid and 7 NL/min exhibited considerably higher β-mannitol peaks and lower δ-mannitol content than other MPs. The comparison between these PXRD profiles and SEM images (Fig. 4) highlighted that the prevalence of β-mannitol led to needle-

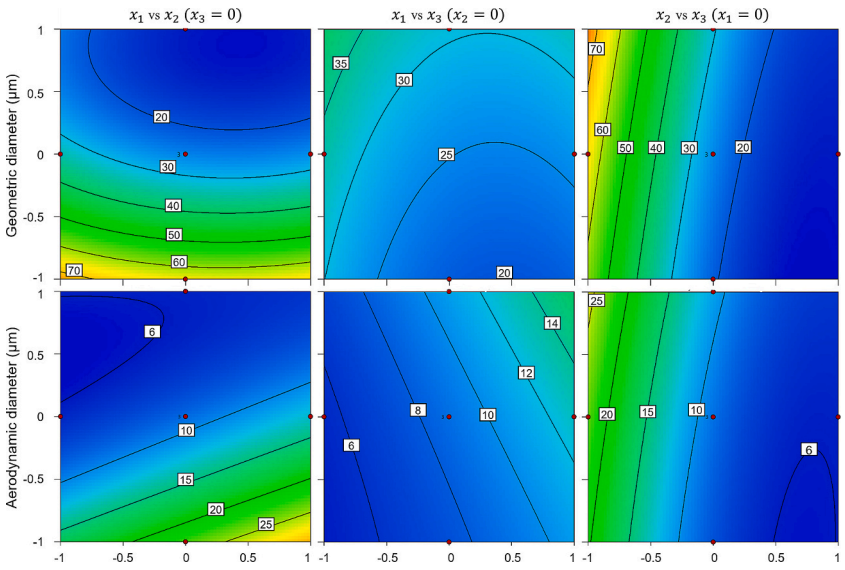

Fig. 6. Contour plots of the mean d_g and $d_{ae}$of MPs produced according to the FCD of F1.

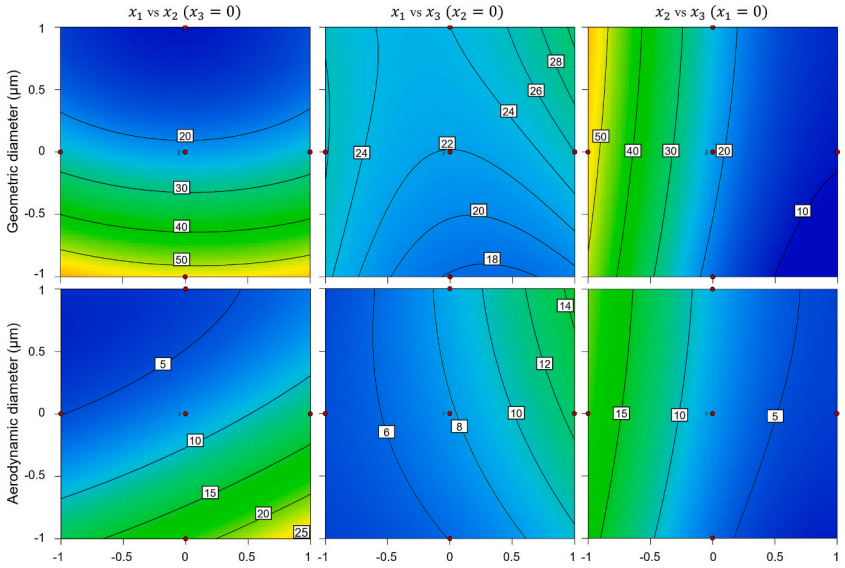

Fig. 7. Contour plots of the mean d_g and $d_{ae}$of MPs produced according to the FCD of F2.

Table 4
Surface tension of four formulations (F1, F2, F2, and F5) prepared at 5 and 20 % (*w/v*) of solid.

Solid % (*w/v*)	Formulation	γ (mN/m)
5	F1	65.1 ± 2.6
20	F1	58.8 ± 0.9
5	F2	61.6 ± 0.8
20	F2	57.4 ± 0.8
5	F3	59.0 ± 0.7
5	F5	57.8 ± 0.4

shaped crystals, while rod-like ones corresponded to the δ-mannitol abundance.

To better quantify the variation of the polymorphic content as a function of the operative conditions, the ratio between characteristic mannitol peaks was investigated. Fig. 9 details the variation of $R_{\delta/\beta}$, $R_{\alpha/\beta}$, and $R_{\alpha/\delta}$ for F1 and F2, with respect to the N_2-to-feed flow rate ratio and the total solid concentration.

The low values of $R_{\alpha/\beta}$, and $R_{\alpha/\delta}$ confirmed that powders were constituted by a mixture of β- and δ-mannitol, while α-mannitol was only present in trace. All the formulations exhibited a common $R_{\delta/\beta}$ profile, where the lowest and the highest values of $R_{\delta/\beta}$ occurred at 7 NL/min and 3 NL/min, respectively. Therefore, significant atomisation gas flow rates corresponded to fewer δ-mannitol and greater β-mannitol formation, while an opposite tendency was detected at moderate N_2 flow rates. Interestingly, a relationship between this trend and the particle size distribution was observed since higher β- and δ-mannitol contents were distinguished at low and high mean d_g, respectively. This phenomenon could be determined by the different freezing time of droplets during the SF process.

Upon atomisation, the nucleation of mannitol crystals may be induced by the creation of supersaturation within the droplet. Indeed, the formation of ice nuclei during freezing may increase the concentration of mannitol in solution (cryoconcentration) thus promoting supersaturation. Therefore, mannitol crystallisation during SF could be a function of the rate of formation of ice crystals within the droplets. Depending on the droplet dimension, ice nucleation (hence, mannitol crystallisation) may start when the droplet is suspended either in the N_2 vapour phase or in the liquid N_2 inducing either slower or faster

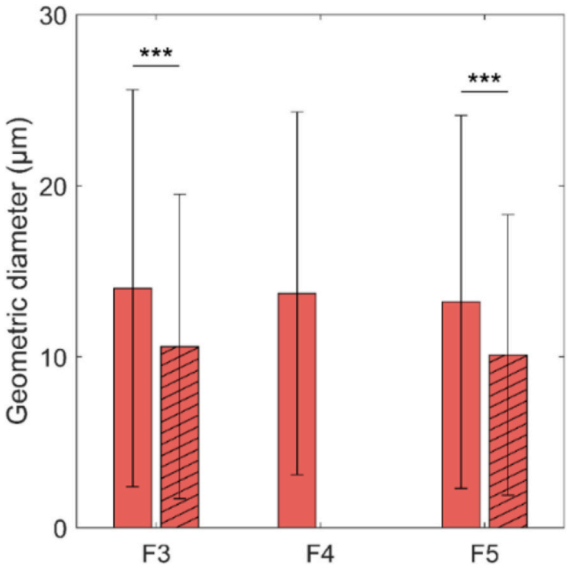

Fig. 8. Geometric diameters expressed as mean ± SD of MPs containing LL at 5 (F3), 10 (F4), and 20 % (*w/w* db) (F5). The filling pattern of bars refers to (none) morphology A, (single diagonal) morphology B. The mean diameters and SD were obtained from a population of 400 MPs. The stars indicate a statistically significant difference (***: $p < 0.001$).

freezing, respectively. Table 5 lists the ice t_n of droplets surrounded by vapour N_2 as a function of their d_g, showing that t_n increased with d_g. It is known that the particle size also influences the time required to achieve the contact between an atomised droplet and the liquid N_2 placed at a fixed distance from the nozzle. Given a distance of 10 cm, 1 ms is necessary for d_g lower than 10 μm while bigger droplets require a smaller time to fall in the liquid [23]. According to Table 5, only the droplets smaller than or equal to 10 μm could have nucleated in the vapour phase since their t_n was inferior to their falling time. In these conditions, the lower driving force of vapour N_2 could have slowed the freezing process, guaranteeing enough time for the formation of β-mannitol due to the Ostwald rule [31]. Bigger droplets, instead, nucleated in the liquid phase at a higher freezing rate, promoting instantaneous freezing and, hence, the formation of metastable δ-mannitol.

3.3.2. *Crystallinity of F3-F5 MPs*

The polymorphism of spray freeze-dried MPs was also assessed in the presence of LL (F3-F5). Fig. 10 displays the PXRD profiles of MPs produced at 5 % (*w/v*) solid, 7 NL/min, and 9 mL/min for different LL concentrations. Compared to LL-free powders, these spectra showed an additional peak at 5.94° indicating the presence of LL, while the

Table 5
Nucleation time t_n of solid inside droplets surrounded by vapour N_2 as a function of their d_g.

d_g (μm)	2	5	10	20	50	100	150
t_n (ms)	0.03	0.14	0.49	1.64	7.72	24.2	46.7

α-mannitol peak at 17.3° disappeared. Both δ- and β-mannitol peaks were present, but β-mannitol at 14.6° and 23.4° was almost absent for F3-F5 formulations. δ-mannitol was the prevalent polymorph for all the investigated conditions, and this result was further confirmed by the analysis of two significative peak ratios, i.e., $R_{\delta/\beta}$ and $R_{\delta/LL}$ (Table 6).

Morphology A showed a broad LL peak (Fig. 10), suggesting the presence of amorphous LL, which was supported by relatively high residual moisture values, i.e., approximately 2 % *w/w* db. Although a mechanistic model was provided for spray drying [20,21], less is known about the crystallisation of LL in SFD. Therefore, to investigate the formation of amorphous LL during SF, it is essential to consider the mechanisms governing particle formation in SFD. When freezing a bicomponent system, the crystallisation of different excipients occurs if their concentration reaches the supersaturation level, which depends on their solubility and concentration [19]. Due to its lower solubility, LL is expected to reach supersaturation before mannitol thus having sufficient time to grow crystals. However, LL concentration of F3-F5 may have not been sufficient for reaching high supersaturation levels within the droplets. Indeed, here, LL was below the threshold concentration of 25 % (*w/w* db) required to achieve its complete crystallisation in SD [20]. Interestingly, as LL concentration increased, $R_{\delta/LL}$ decreased while $I_{5.94°}$ increased. Moreover, the LL peak area normalised to the mass of LL in the formulation increased with LL concentration (data not shown), highlighting an increasing proportion between crystalline and amorphous LL. This indicated a greater crystallisation of LL as its content increased, likely driven by the faster achievement of supersaturation within the freezing droplet at higher LL concentrations [20]. On the other hand, mannitol could have crystallised before LL due to its high concentration between 79 % and 94 % (*w/w* db). The fast crystallisation of mannitol could also have interfered with LL crystallisation, as observed in the presence of trehalose in spray dried MPs [33].

Morphology B, instead, displayed higher mannitol peaks and sharper LL peaks, whose intensity increased again with LL concentration. Therefore, the comparison of the two morphologies at equal amino acid content pointed out a greater crystallisation of mannitol and LL in morphology B than in morphology A. The greater crystallisation of LL could explain the rougher surface of morphology B compared to morphology A (Fig. 3) [18]. LL tends to accumulate at the MPs' surface due to its surfactant properties and LL crystals reportedly increase the surface roughness of spray-dried MPs [26]. Instead, the reduced crystallisation of LL in morphology A is associated with the smoother surface (Fig. 3). Since powder manufacturing was consistent, the formation of

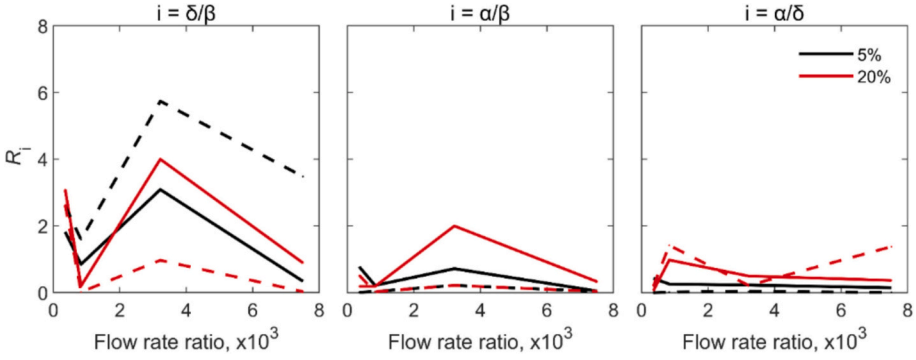

Fig. 9. $R_{\delta/\beta}$, $R_{\alpha/\beta}$, and $R_{\alpha/\delta}$ of MPs produced at 5, 20 % (*w/v*) of solid (F1 and F2) and different N_2-to-feed flow rate ratios. Solid lines refer to mannitol alone (F1), while dashed lines refer to mannitol +1 % (*w/w* db) SS (F2).

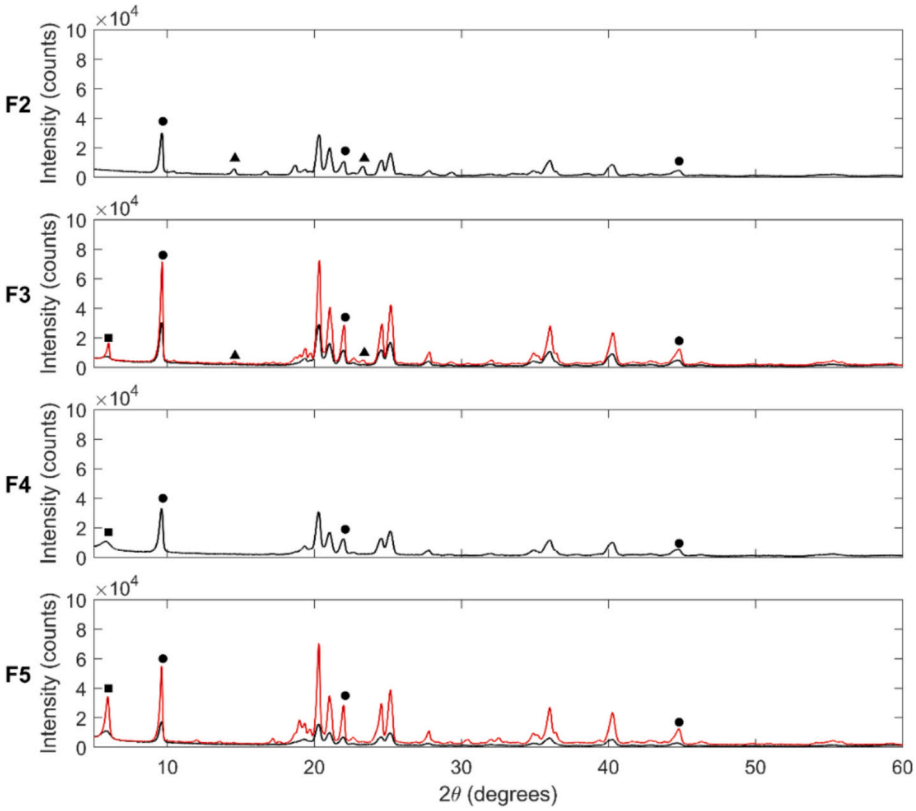

Fig. 10. PXRD patterns of MPs devoid and containing LL at 5 (F3), 10 (F4), and 20 % (*w/w* db) (F5). Peaks relative to either LL or a specific mannitol polymorph are marked with a different symbol: (■) LL, (▲) β-mannitol, and (●) δ-mannitol. Black lines refer to morphology A, while red lines refer to morphology B. MPs were produced at 5 % (*w/v*) solid, 7 NL/min, and 9 mL/min. (For interpretation of the references to colour in this figure legend, the reader is referred to the web version of this article.)

Table 6
$R_{\delta/\beta}$, $R_{\delta/LL}$ and aerosolization properties of MPs devoid and containing LL at 5 (F3), 10 (F4), and 20 % (*w/w* db) (F5). MPs were produced at 5 % (*w/v*) solid, 7 NL/min, and 9 mL/min. The aerosolization data were presented as mean ± SD ($n = 3$).

	Morphology	$R_{\delta/\beta}$	$R_{\delta/LL}$	EF (%)	FPF (%)	MMAD (μm)	GSD (−)
F2	–	1.6	–	83.8 ± 3.6	23.6 ± 4.9	4.5 ± 0.2	2.2 ± 0.1
F3	A	24.8	4.1	83.1 ± 2.3	39.8 ± 3.7	2.4 ± 0.1	2.4 ± 0.1
F3	B	18.0	2.1	92.1 ± 0.9	21.4 ± 4.1	4.8 ± 0.3	2.1 ± 0.1
F4	A	∞	2.1	88.8 ± 1.7	48 ± 3	2.0 ± 0.1	3.2 ± 0.1
F5	A	∞	1	95.5 ± 2.3	43.2 ± 7.5	3.5 ± 1.1	4.3 ± 0.7
F5	B	33.8	0.9	93.2 ± 1.1	15.8 ± 4.3	5.1 ± 0.6	2.4 ± 0.1

morphology B might be ascribable to a recrystallization of the powders during storage associated with the presence of amorphous materials [34]. Indeed, the presence of amorphous LL after SFD could have triggered its transition to crystalline LL (morphology B) [18]. Recrystallization is a common phenomenon in pharmaceutical dry powders, which could potentially alter their aerodynamics [18]. Residual amounts of disordered amorphous LL were also identified as responsible for the recrystallization of spray dried LL during storage [28].

3.4. In vitro drug deposition

As discussed above, the FCD highlighted the combination 5 % (*w/v*) solid, 7 NL/min, and 9 mL/min as the optimal one. Therefore, the aerosolization properties of MPs produced under these operative conditions were studied for the formulations F2-F5 via NGI. Table 6 details the EF, FPF, MMAD, and GSD of four powders, i.e., without and with LL at 5, 10, and 20 % (*w/w* db). The EF generally increased with the amino acid amount and in the presence of morphology B. The addition of LL combined with the formation of morphology B decreased the FPF from 23.6 ± 4.9 % to 21.4 ± 4.1 % and 15.8 ± 4.3 % at 5 and 20 % (*w/w* db) LL, respectively. Accordingly, the MMAD increased from 4.5 ± 0.2 μm to 4.8 ± 0.3 μm and 5.1 ± 0.6 μm. This tendency could be ascribable to the significant cohesiveness of morphology B MPs, whose dense degree of packing could have adversely affected their flowability. In addition, the poor aerodynamics may have been caused by a shrinkage of MPs during storage (due to the recrystallization) leading to a closer porous structure and higher MPs' densities. This theory was also coherent with the smaller mean d_g possessed by morphology B MPs compared to morphology A MPs (Fig. 8). On the contrary, the presence of morphology A improved the aerodynamic properties of MPs by increasing both the FPF and the MMAD. Indeed, the formation of morphology A during SFD allowed for the reduction of MPs cohesiveness, preventing their packing, and enhancing their aerodynamics. In particular, the maximum FPF (48 ± 3 %) and the minimum MMAD (2.0 ± 0.1 μm) were achieved for the formulation F4.

These outcomes were supported by the in vitro drug deposition profiles, based on the recovery of SS in each stage of the NGI. Fig. 11 compares the aerodynamic behaviour of F2-F5 in the presence of morphology A. The percentage of powders recovered in the NGI cups (S1-MOC) was 35.0 ± 3.5 %, 41.3 ± 4.5 %, 55.3 ± 3.2 %, and 65.5 ± 1.9 % for F2, F3, F4, and F5, respectively. Hence, the increase in amino acid content gradually reduced the RF in DEV, IP, and PRE, while the highest deposition in the deepest stages was obtained for F4.

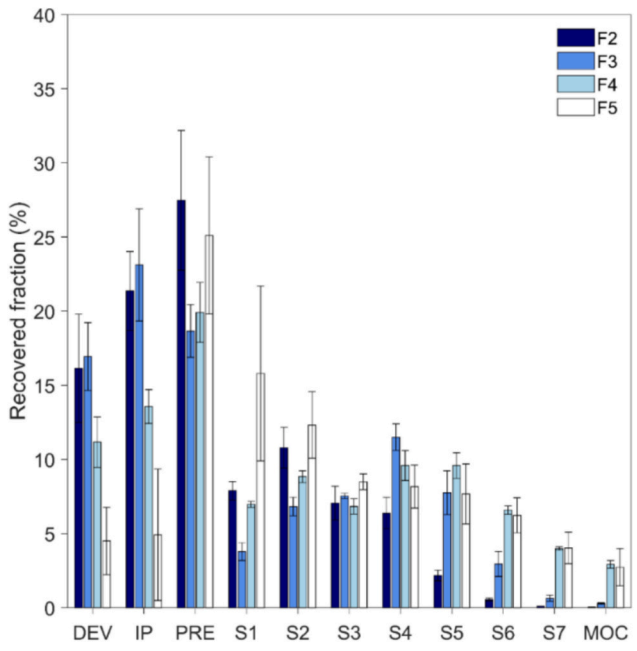

Fig. 11. In vitro deposition profiles of MPs devoid and containing LL at 5 (F3), 10 (F4), and 20 % (*w/w* db) (F5). MPs were produced at 5 % (*w/v*) solid, 7 NL/min, and 9 mL/min and showed the morphology 'morphology A' upon the addition of LL.

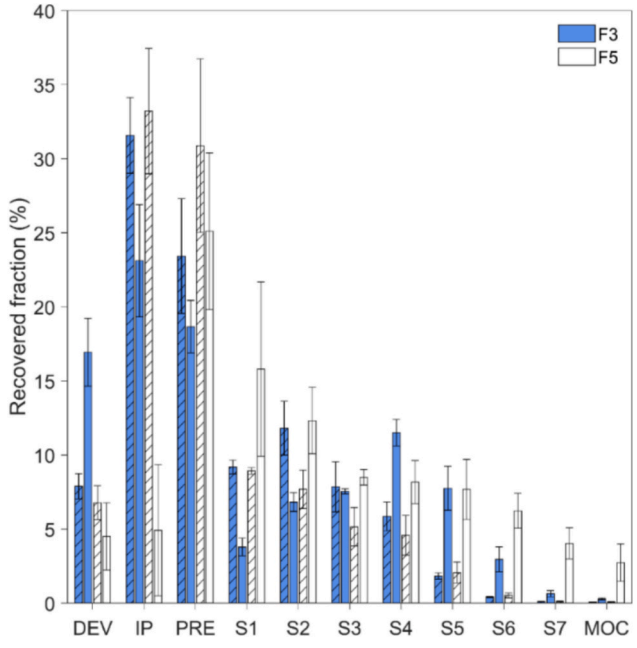

Fig. 12. In vitro deposition profiles of MPs containing LL at 5 (F3) and 20 % (*w/w* db) (F5), produced at 5 % (*w/v*) solid, 7 NL/min, and 9 mL/min. The filling pattern of bars refers to (none) morphology A, (single diagonal) morphology B.

The comparison between the deposition pattern of SS for morphology A and B is reported in Fig. 12. Contrary to morphology A, the fraction of SS recovered between S1 and MOC decreased for growing LL concentration, being the F2 and F3 RF equal to 37.1 ± 4.3 % and 29.1 ± 4.8 %, respectively. Therefore, the aerodynamic performance of powders was jeopardized by the presence of morphology B despite its lower geometric size.

In conclusion, a dependency of the aerosolization properties on the crystallinity of LL and mannitol was highlighted. These results support the hypothesis positing the variation of LL's mechanism of action between SFD and SD [17]. Indeed, morphology B exhibited the worst flowability in the presence of highly crystalline LL and corrugated surfaces, while the best aerodynamics was achieved when the recrystallization of mannitol and LL was avoided, inducing lower cohesiveness. An opposite behaviour was displayed by spray dried MPs, whose flowability was boosted by LL crystallisation and surface corrugation [20].

4. Conclusions

This work employed a face centered design to investigate the influence of the process variables on the particle size of spray freeze-dried mannitol MPs. Overall, the d_g decreased for growing N_2 flow rates and solid concentrations, while it increased with the feed flow rate. The d_{ae} showed equal tendencies except for its increase at growing solid concentrations. Furthermore, the addition of SS led to a reduced particle size due to the lower surface tension. The crystallinity of MPs appeared to change with the N_2 flow rate, leading to a prevalence of δ-mannitol at high values and a superior amount of β-mannitol at low flow rates. This phenomenon shed light on the relationship between particle size, freezing time and polymorphism. Moreover, the incorporation of LL into the MPs led to the formation of two morphologies with different degree of crystallinity. One was formed by highly crystalline mannitol (δ + β) and LL, while the other one possessed a lower crystallinity and exhibited only δ-mannitol. The higher crystallinity induced by recrystallization led to the formation of more irregular MPs, affected by elevated cohesion forces and with poor flowability. Instead, a lower crystallinity significantly improved the aerosolization properties of MPs up to maximum FPF (48 %) and MMAD (2 μm) at 10 % (*w/w* db) LL. This result disclosed the influence of polymorphism on the MPs' cohesiveness, proving the dependency of the MPs' aerodynamics on LL and mannitol crystallinity. Moreover, the influence of LL crystallinity on inter-particle cohesiveness provides further information on the mechanism of action of LL in SFD. By contrast, the control of recrystallization during storage in the presence of crystalline excipients such as mannitol and LL was beyond the scope of this work and will be material of further studies.

Funding

This publication is part of the project PNRR-NGEU, which has received funding from the MUR-DM352/2022. This research was funded by Chiesi Farmaceutici S.p.A.

CRediT authorship contribution statement

Lorena Pasero: Writing – original draft, Visualization, Validation, Methodology, Formal analysis, Data curation, Conceptualization. **Adamo Sulpizi:** Writing – review & editing, Supervision, Resources, Methodology, Conceptualization. **Tomaso Guidi:** Writing – review & editing, Resources, Project administration, Funding acquisition, Conceptualization. **Roberto Pisano:** Writing – review & editing, Supervision, Resources, Project administration, Methodology, Funding acquisition, Conceptualization.

Declaration of competing interest

Lorena Pasero holds a Doctorate Studentship and collaborates with Chiesi Farmaceutici S.p.A as part of her PhD training. Adamo Sulpizi and Tomaso Guidi are employees of Chiesi Farmaceutici S.p.A. All authors declare no conflicts of interest.

Acknowledgments

The authors are grateful to Angelo Carini (Chiesi Farmaceutici S.p.

A.) for supporting us in the use of the NGI.

Appendix A. Supplementary data

Supplementary data to this article can be found online at https://doi.org/10.1016/j.powtec.2025.120788.

Data availability

Data not available.

References

[1] M.B. Adali, A.A. Barresi, G. Boccardo, R. Pisano, Spray Freeze-Drying as a Solution to Continuous Manufacturing of Pharmaceutical Products in Bulk, 2020, https://doi.org/10.3390/PR8060709.

[2] T. Duong, et al., A Pathway from Porous Particle Technology toward Tailoring Aerogels for Pulmonary Drug Administration, 2021, https://doi.org/10.3389/fbioe.2021.671381.

[3] S. Wanning, R. Süverkrüp, A. Lamprecht, Pharmaceutical spray freeze drying, Int. J. Pharm. 488 (1–2) (Jul. 2015) 136–153, https://doi.org/10.1016/j.ijpharm.2015.04.053.

[4] S.M. D'Addio, J.G.Y. Chan, P.C.L. Kwok, R.K. Prud'Homme, H.K. Chan, Constant size, variable density aerosol particles by ultrasonic spray freeze drying, Int. J. Pharm. 427 (2) (May 2012) 185–191, https://doi.org/10.1016/j.ijpharm.2012.01.048.

[5] D.A. Vishali, J. Monisha, S.K. Sivakamasundari, J.A. Moses, C. Anandharamakrishnan, Spray freeze drying: emerging applications in drug delivery, J. Control. Release 300 (Apr. 2019) 93–101, https://doi.org/10.1016/j.jconrel.2019.02.044.

[6] R.O. Williams, T.C. Carvalho, J.I. Peters, Influence of Particle Size on Regional Lung Deposition - What Evidence Is There?, 2011, https://doi.org/10.1016/j.ijpharm.2010.12.040.

[7] L. Pasero, F. Susa, T. Limongi, R. Pisano, A review on micro and nanoengineering in powder-based pulmonary drug delivery, Int. J. Pharm. (May 2024) 124248, https://doi.org/10.1016/j.ijpharm.2024.124248.

[8] B. Chaurasiya, Y.Y. Zhao, Dry Powder for Pulmonary Delivery: A Comprehensive Review, 2021, https://doi.org/10.3390/pharmaceutics13010031.

[9] A.R. Parsian, A. Vatanara, M.R. Rahmati, K. Gilani, K.M. Khosravi, A.R. Najafabadi, Inhalable budesonide porous microparticles tailored by spray freeze drying technique, Powder Technol. 260 (2014) 36–41, https://doi.org/10.1016/j.powtec.2014.03.043.

[10] Q. Liao, et al., Porous and highly dispersible voriconazole dry powders produced by spray freeze drying for pulmonary delivery with efficient lung deposition, Int. J. Pharm. 560 (2019), https://doi.org/10.1016/j.ijpharm.2019.01.057.

[11] M.R. Rahmati, et al., Effect of formulation ingredients on the physical characteristics of salmeterol xinafoate microparticles tailored by spray freeze drying, Adv. Powder Technol. 24 (1) (Jan. 2013) 36–42, https://doi.org/10.1016/j.apt.2012.01.007.

[12] D.M. Haghighi, H. Faghihi, M. Darabi, M.S. Mirmoeini, A. Vatanara, Spray freeze drying to solidify Nanosuspension of Cefixime into inhalable microparticles, DARU J. Pharm. Sci. 30 (1) (Jun. 2022) 17–27, https://doi.org/10.1007/s40199-021-00426-4.

[13] M.A. Pouya, B. Daneshmand, S. Aghababaie, H. Faghihi, A. Vatanara, Spray-freeze drying: a suitable method for aerosol delivery of antibodies in the presence of Trehalose and Cyclodextrins, AAPS PharmSciTech 19 (5) (Jul. 2018) 2247–2254, https://doi.org/10.1208/s12249-018-1023-2.

[14] L. Pasero, et al., Tailoring dry microparticles for pulmonary drug delivery: ultrasonic spray freeze-drying with mannitol and salbutamol sulphate, Processes 11 (11) (Oct. 2023) 3096, https://doi.org/10.3390/pr11113096.

[15] T. Ye, J. Yu, Q. Luo, S. Wang, H.-K. Chan, Inhalable clarithromycin liposomal dry powders using ultrasonic spray freeze drying, Powder Technol. 305 (Jan. 2017) 63–70, https://doi.org/10.1016/j.powtec.2016.09.053.

[16] W. Liang, M.Y.T. Chow, S.F. Chow, H.K. Chan, P.C.L. Kwok, J.K.W. Lam, Using two-fluid nozzle for spray freeze drying to produce porous powder formulation of naked siRNA for inhalation, Int. J. Pharm. 552 (1–2) (2018), https://doi.org/10.1016/j.ijpharm.2018.09.045.

[17] H. Otake, T. Okuda, D. Hira, H. Kojima, Y. Shimada, H. Okamoto, Inhalable spray-freeze-dried powder with L-leucine that delivers particles independent of inspiratory flow pattern and inhalation device, Pharm. Res. 33 (4) (Apr. 2016) 922–931, https://doi.org/10.1007/s11095-015-1838-4.

[18] L. Li, et al., Investigation of L-leucine in reducing the moisture-induced deterioration of spray-dried salbutamol sulfate power for inhalation, Int. J. Pharm. 530 (1–2) (Sep. 2017) 30–39, https://doi.org/10.1016/j.ijpharm.2017.07.033.

[19] M.A. Boraey, S. Hoe, H. Sharif, D.P. Miller, D. Lechuga-Ballesteros, R. Vehring, Improvement of the dispersibility of spray-dried budesonide powders using leucine in an ethanol-water cosolvent system, Powder Technol. 236 (Feb. 2013) 171–178, https://doi.org/10.1016/j.powtec.2012.02.047.

[20] A.L. Feng, M.A. Boraey, M.A. Gwin, P.R. Finlay, P.J. Kuehl, R. Vehring, Mechanistic models facilitate efficient development of leucine containing microparticles for pulmonary drug delivery, Int. J. Pharm. 409 (1–2) (May 2011) 156–163, https://doi.org/10.1016/j.ijpharm.2011.02.049.

[21] R. Vehring, W.R. Foss, D. Lechuga-Ballesteros, Particle formation in spray drying, J. Aerosol Sci. 38 (7) (2007) 728–746, https://doi.org/10.1016/j.jaerosci.2007.04.005.

[22] J.D. Berry, M.J. Neeson, R.R. Dagastine, D.Y.C. Chan, R.F. Tabor, Measurement of Surface and Interfacial Tension using Pendant Drop Tensiometry, Academic Press Inc, Sep. 05, 2015, https://doi.org/10.1016/j.jcis.2015.05.012.

[23] K. Al-Hakim, G. Wigley, A.G.F. Stapley, Phase doppler anemometry studies of spray freezing, Chem. Eng. Res. Des. 84 (12 A) (2006) 1142–1151, https://doi.org/10.1205/cherd06014.

[24] R.H. Perry, Perry's Chemical Engineers' Handbook, 6th ed., McGraw-Hill, New York, 1984.

[25] H. Jain, A. Bairagi, S. Srivastava, S.B. Singh, N.K. Mehra, Recent Advances in the Development of Microparticles for Pulmonary Administration, 2020, https://doi.org/10.1016/j.drudis.2020.07.018.

[26] N. Alhajj, N.J. O'Reilly, H. Cathcart, Leucine as an Excipient in Spray Dried Powder for Inhalation, Elsevier Ltd, Oct. 01, 2021, https://doi.org/10.1016/j.drudis.2021.04.009.

[27] D. Lechuga-Ballesteros, et al., Trileucine improves aerosol performance and stability of spray-dried powders for inhalation, J. Pharm. Sci. 97 (1) (2008) 287–302, https://doi.org/10.1002/jps.21078.

[28] K. Kramm, et al., Influence of nozzle parameters on spray pattern and droplet characteristics for a two-fluid nozzle, Chem. Ing. Tech. 95 (1–2) (Jan. 2023) 151–159, https://doi.org/10.1002/cite.202200152.

[29] J. Raula, et al., Investigations on the humidity-induced transformations of salbutamol sulphate particles coated with L-leucine, Pharm. Res. 25 (10) (Oct. 2008) 2250–2261, https://doi.org/10.1007/s11095-008-9613-4.

[30] Y. Yang, J. Liu, A. Hu, T. Nie, Z. Cheng, W. Liu, A Critical Review on Engineering of d-Mannitol Crystals: Properties, Applications, and Polymorphic Control, MDPI, Aug. 01, 2022, https://doi.org/10.3390/cryst12081080.

[31] Y.Y. Lee, J.X. Wu, M. Yang, P.M. Young, F. Van Den Berg, J. Rantanen, Particle size dependence of polymorphism in spray-dried mannitol, Eur. J. Pharm. Sci. (Sep. 2011) 41–48, https://doi.org/10.1016/j.ejps.2011.06.002.

[32] S. Yan, S. Zhang, X.D. Chen, W.D. Wu, Spray freeze dried uniform mannitol microspheres, Powder Technol. 434 (Feb. 2024), https://doi.org/10.1016/j.powtec.2023.119312.

[33] M. Ordoubadi, et al., On the particle formation of leucine in spray drying of inhalable microparticles, Int. J. Pharm. 592 (Jan. 2021), https://doi.org/10.1016/j.ijpharm.2020.120102.

[34] T. Yoshinari, R.T. Forbes, P. York, Y. Kawashima, Moisture induced polymorphic transition of mannitol and its morphological transformation, Int. J. Pharm. 247 (2002) 69–77, https://doi.org/10.1016/S0378-5173(02)00380-0PMID:12429486.